DTIC FILE COPY

(4)

REPORT SD-TR-87-57

AD-A193 004

Ultraviolet-Visible Spectroscopy of Laser-Produced Aluminum Plasmas

J. T. KNUDTSON, W. B. GREEN and D. G. SUTTON
Aerophysics Laboratory
Laboratory Operations
The Aerospace Corporation
El Segundo, CA 90245-4691

22 January 1988

Final Report

Prepared for

SPACE DIVISION
AIR FORCE SYSTEMS COMMAND
Los Angeles Air Force Base
P.O. Box 92960, Worldway Postal Center
Los Angeles, CA 90009-2960

DTIC
ELECTE
MAR 3 0 1988
S D
D

APPROVED FOR PUBLIC RELEASE.
DISTRIBUTION UNLIMITED

88 3 29 099

This report was submitted by The Aerospace Corporation, El Segundo, CA 90245, under Contract No. F04701-85-C-0086 with the Space Division, P. O. Box 92960, Worldway Postal Center, Los Angeles, CA 90009-2960. It was reviewed and approved for The Aerospace Corporation by W. P. Thompson, Jr., Director, Aerophysics Laboratory.

Lt Scott W. Levinson/CNW was the Air Force project officer for the Mission-Oriented Investigation and Experimentation (MOIE) Program.

This report has been reviewed by the Public Affairs Office (PAS) and is releasable to the National Technical Information Service (NTIS). At NTIS, it will be available to the general public, including foreign nationals.

This technical report has been reviewed and is approved for publication. Publication of this report does not constitute Air Force approval of the report's findings or conclusions. It is published only for the exchange and stimulation of ideas.

SCOTT W. LEVINSON, Lt, USAF
MOIE Project Officer
SD/CNW

JOSEPH HESS, GM-15
Director, AFSTC West Coast Office
AFSTC/WCO OL-AB

PAGES _____

ARE

MISSING

IN

ORIGINAL

DOCUMENT

UNCLASSIFIED
SECURITY CLASSIFICATION OF THIS PAGE

A193 004

REPORT DOCUMENTATION PAGE

1a. REPORT SECURITY CLASSIFICATION Unclassified	1b. RESTRICTIVE MARKINGS
2a. SECURITY CLASSIFICATION AUTHORITY 2b. DECLASSIFICATION / DOWNGRADING SCHEDULE	3. DISTRIBUTION / AVAILABILITY OF REPORT Approved for public release; distribution unlimited.
4. PERFORMING ORGANIZATION REPORT NUMBER(S) TR-0086(6930-01)-14	5. MONITORING ORGANIZATION REPORT NUMBER(S) SD-TR-87-57
6a. NAME OF PERFORMING ORGANIZATION The Aerospace Corporation Laboratory Operations 6b. OFFICE SYMBOL (If applicable)	7a. NAME OF MONITORING ORGANIZATION Space Division
6c. ADDRESS (City, State, and ZIP Code) El Segundo, CA 90245	7b. ADDRESS (City, State, and ZIP Code) Los Angeles Air Force Base Los Angeles, CA 90009-2
8a. NAME OF FUNDING / SPONSORING ORGANIZATION 8b. OFFICE SYMBOL (If applicable)	9. PROCUREMENT INSTRUMENT IDENTIFICATION NUMBER F04701-85-C-0086
8c. ADDRESS (City, State, and ZIP Code)	10. SOURCE OF FUNDING NUMBERS PROGRAM ELEMENT NO. / PROJECT NO. / TASK NO. / WORK UNIT ACCESSION NO.

11. TITLE (Include Security Classification)
Ultraviolet-Visible Spectroscopy of Laser-Produced Aluminum Plasmas

12. PERSONAL AUTHOR(S)
Knudtson, J. Thomas, Green, William B., and Sutton, David G.

13a. TYPE OF REPORT	13b. TIME COVERED FROM ____ TO ____	14. DATE OF REPORT (Year, Month, Day)	15. PAGE COUNT
		1988 January 22	46

16. SUPPLEMENTARY NOTATION

17 COSATI CODES			18 SUBJECT TERMS (Continue on reverse if necessary and identify by block number)
FIELD	GROUP	SUB-GROUP	Laser effects, Laser produced plasma Plasma spectroscopy

19. ABSTRACT (Continue on reverse if necessary and identify by block number)

The optical emission spectra (180 to 760 nm) of plasmas produced by a flashlamp-pumped dye laser focused on an aluminum target have been recorded and analyzed. In the incident intensity range from near plasma threshold to 5×10^{7} W/cm^2, the electron temperature was calculated from the relative emission intensity of Al(II) states ($T_e = 8.0 \times 10^3$ K). The electron density was determined from Stark broadened linewidths of four Al(II) lines. Both the spatial and temporal dependence of the emission spectra were obtained, providing a map of the electron density and temperature.

20. DISTRIBUTION / AVAILABILITY OF ABSTRACT ☐ UNCLASSIFIED/UNLIMITED ☒ SAME AS RPT ☐ DTIC USERS	21. ABSTRACT SECURITY CLASSIFICATION Unclassified
22a NAME OF RESPONSIBLE INDIVIDUAL	22b TELEPHONE (Include Area Code) / 22c OFFICE SYMBOL

DD FORM 1473, 84 MAR — 83 APR edition may be used until exhausted. All other editions are obsolete.

SECURITY CLASSIFICATION OF THIS PAGE
UNCLASSIFIED

PREFACE

The authors gratefully acknowledge essential equipment loans from S. Amimoto, R. Heidner, K. Herr, B. Koffend, and M. Lundquist, and stimulating discussions with R. Gross, H. Helvajian, E. Weitz, and A. Woodin.

Accession For
NTIS CRA&I
DTIC TAB
Unannounced
Justification
By
Distribution/
Availability Codes
Dist | Avail and/or Special
A-1

CONTENTS

PREFACE 1

I. INTRODUCTION 7

II. EXPERIMENT 9

III. RESULTS 17

A. Emission Spectrum 17

B. Spatial and Temporal Dependence of Plasma Emission 17

C. Electron Temperature from Al (II) Emission 23

D. Electron Densities 31

E. Temperature and Electron Densities as a Function of Time and Position 35

F. Continuum Emission Spectrum at z = 0 mm 35

IV. DISCUSSION 41

V. CONCLUSIONS 45

REFERENCES 47

FIGURES

1. Apparatus for plasma emission spectroscopy..... 10

2. Flashlamp-pumped dye laser pulse shape..... 10

3. OMA-monochromator field of view relative to target surface..... 13

4. Focused beam profile at target surface..... 14

5. Depth profile of laser-produced crater..... 15

6. Plasma emission spectrum from 180 nm to 340 nm..... 18

7. Plasma emission spectrum from 340 nm to 500 nm..... 19

8. Plasma emission spectrum from 540 nm to 640 nm..... 20

9. Plasma emission spectrum from 680 nm to 760 nm..... 21

10. Plasma emission spectrum in 460-nm region at five distances from the target surface..... 22

11. Emissivity of 466-nm Al(II) emission line as a function of distance from the target for two delay times..... 24

12. Partial energy level diagram for Al(II) showing transitions used for temperature calculations..... 26

13. Relative emissivities corrected for degeneracy and radiative rate versus energy of upper state..... 28

14. The 460-nm spectral region at three laser intensities..... 30

15. The Al(II) 466.3-nm emission line at 1.27 mm from the target surface and 1-μs delay time..... 32

16. Electron temperature and plasma electron densities derived from the Stark-broadened 466.3-nm line as a function of distance from the target and 1-μs delay time..... 36

17. The Al(II) temperature and electron density derived from the 466.3-nm Stark-broadened linewidth at three delay times..... 37

18. Plasma emission spectrum at 5.3×10^7 W/cm^2, 0 mm from target surface, and 1-μs delay time..... 38

TABLES

I. Parameters for Electron Temperature Calculations..... 27

II. Laser Intensity Dependence of T_e and N_e..... 29

III. Stark Broadened Linewidths..... 33

I. INTRODUCTION

A laser pulse focused on an opaque surface can produce high heating rates and high temperatures. At low intensities, heating without a phase change occurs. With a higher intensity pulse, the target material melts and/or vaporizes. These regimes have been successfully modeled with differential equations describing the heat flow at the target surface.[1] At even higher laser intensities ionization occurs, which can lead to plasma formation. The production and nature of laser produced plasmas (LPPs) are more difficult to model. The readily observable optical emission from an LPP is useful in characterizing both the laser target interaction and the resulting plasma.

The emission spectrum of an LPP depends on the techniques used to observe it.[2,3] Many previous studies viewed the entire plasma (spatial integration), and frequently with film (temporal integration). Spectroscopy of an LPP using a CO_2 laser and an aluminum target in vacuum[4] and in air[5,6] has been reported. The relatively long, microsecond laser pulsewidths permitted time resolved results in some cases. With short pulse (50 ns) excimer lasers, time integrated spectroscopy has been reported.[7] The thermal and mechanical effects of a microsecond-pulsewidth excimer laser have been investigated and successfully modeled.[8,9] Irons and coworkers have published a series of detailed investigations of the temporal, spatial, and spectral characteristics of a plasma generated on a polyethylene film by a pulsed ruby laser.[10]

In the work reported here, we use both spatial and temporal resolution to record the emission spectrum of an LPP formed on an aluminum surface by a flashlamp-pumped dye laser. Analysis of the spectra provides useful plasma parameters. Relative ion emission intensities provide electron temperatures, and Stark broadened linewidths yield electron densities. These are reported as a function of time, distance from target, and incident laser intensity.

II. EXPERIMENT

A top view of the experimental apparatus is shown in Fig. 1. A Candela flashlamp-pumped dye laser was operated with Rhodomine 6G dye in a 1:1, H_2O/MeOH solvent without any dispersive elements in the cavity. The temporal profile of the pulse, taken with a biplanar photodiode, is shown in Fig. 2. Reproducible laser pulses of up to 2 J were obtained at 583 nm. Inside the vacuum chamber, a 15-cm focal length CaF_2 lens (L1) focused the laser on the aluminum (alclad 2024) target, which was mounted on an x-y translator to provide unexposed material for each laser pulse. The vacuum chamber was pumped down to 10^{-2} Torr.

CaF_2 lenses, L2 (inside the vacuum chamber) and L3 (outside the vacuum chamber), relayed the image (magnification = 1) of the plasma onto the slits of a 2/3 meter McPherson monochromator. Both windows in the vacuum chamber were CaF_2.

A gated (20 ns) image-intensified optical multichannel analyzer (OMA) (PAR OMA III with 1420B detector) viewed the output plane of the monochromator. With a 600 ℓ/mm grating, about 40 nm of the optical spectrum was obtained in a single shot (dispersion = 2.48 nm/mm). Timing for the gate was derived from a photodiode viewing the target. A variable delay generator allowed adjustment of the OMA gate with respect to the leading edge of the laser pulse.

The monochromator-OMA spectral sensitivity was calibrated using a quartz-halogen lamp (GE 6.6A/T4Q/1CL-200 W) and its published spectral radiance.[11] The color temperature of the lamp was measured (2750°C) with an optical pyrometer prior to calibration. We extrapolated the published radiance for the 180- to 250-nm region and, therefore, the emission intensity recorded in this region is only approximate. In all the spectra reported here, the dark current counts from the detector were taken immediately following the laser pulse and subtracted from the emission spectrum.

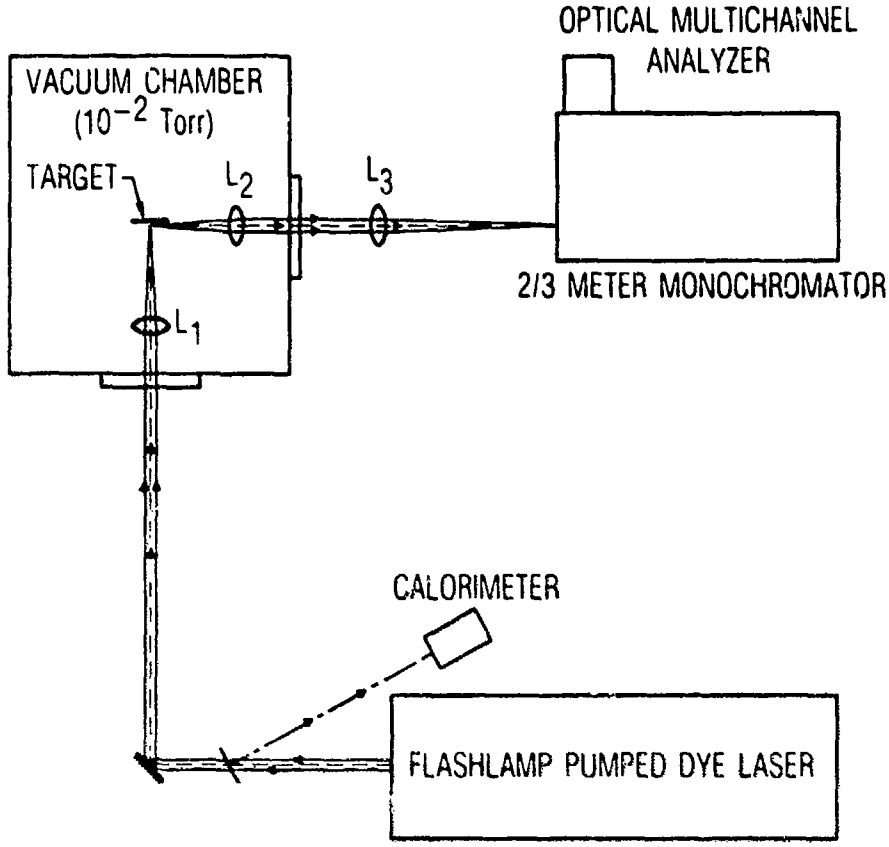

Fig. 1. Apparatus for Plasma Emission Spectroscopy. L1 (15-cm focal length) focuses the laser on the target. L2 and L3 relay the image of the laser-produced plasma onto the slits of the monochromator.

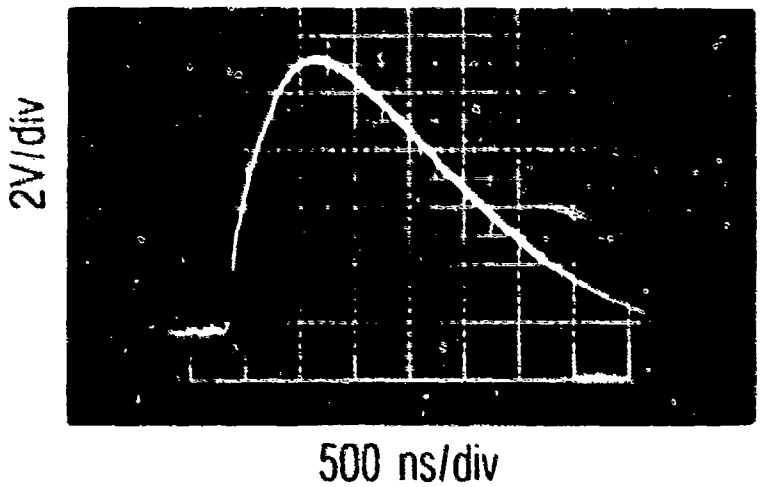

Fig. 2. Flashlamp-pumped dye-laser pulse shape

The observed plasma emission is most readily interpreted if the detector views a homogeneous region of the plasma. Figure 3 shows how the laser beam profile was matched to the detector field of view to achieve this. In Fig. 3 the laser beam propagates from right to left along the z axis, which is perpendicular to the target plane. The monochromator slits are parallel to the target surface. (The image relaying lenses of Fig. 1 have been removed for simplicity.) As shown by the cross-hatched region of the slit, the OMA detector views only a 1-mm portion of the available slit height. The laser beam diameter was adjusted so that its full width at half height (fwhh) exactly matched the field of view of the detector. Since the laser spatial profile was approximately top hat (see below) the detection system viewed a homogeneous slice (at some distance along the z axis) of the cylindrically symmetric LPP.

The monochromator-OMA system was mounted on precision translators that allowed the monochromator (slit) to be scanned across the image of the LPP in the z direction. The entrance slit width was typically 50 μm. The overall wavelength resolution was limited by the OMA's spatial resolution and was measured to be 0.23 nm with an He-Ne laser.

Since fluence is an important parameter, both the energy on target and its spatial distribution were carefully measured. The laser energies used in this study were obtained by placing a calorimeter (Scientech) immediately following the focusing lens. The spatial distribution was measured with a linear diode array (Reticon RL-1024S) with 25-μm resolution. A typical beam profile is shown in Fig. 4. It is approximately top hat with some modulation on the peak. For all fluence calculations, the area was 7.9×10^{-3} cm^2, based on a measured diameter of 1.0 mm, as shown in Fig. 4. The small spike to the right of the laser profile is an inoperative pixel in the array and represents the resolution (0.025 mm) of the profile.

The craters formed by the focused laser were characterized using a Dektac profilometer. A typical crater profile resulting from a 0.82-J (on target) laser pulse is shown in Fig. 5. The diameter of the crater, 1.0 mm, is in good agreement with the laser beam profile measurement in Fig. 4. At the edge

of the crater, there is a ridge about 10 μm high. It was apparently formed by molten aluminum that was forced out of the crater and subsequently cooled. Since the crater was circularly symmetric, we can estimate the mass of aluminum removed by the laser pulse from the crater profile and aluminum density (2.77 g/cm^3). Several craters were profiled, and the average volume was 1×10^{-5} cm^3, corresponding to the removal of 30 μg of aluminum.

In the low-laser-intensity regime, the crater depth can be calculated with a simple model based on the thermal diffusivity k of the target.[1] When heat is applied to a thin plate for time τ, the distance over which the temperature is the same order of magnitude is D.

$$D = (4k\tau)^{1/2}$$

Using the fwhh of the laser pulse (2 μs) and k = 0.93 cm^2/sec for aluminum, the calculated depth is 27 μm. The crater depth in Fig. 5 ranges from 20 to 30 μm.

The initial absorption of the laser beam results from the absorptance of 0.21 of the 0.0165-in.-thick Alclad 2024 samples. (A reflectance of 0.79 was measured with a Beckman diffuse reflectance spectrometer at 580 nm). As the target is heated, the absorptance increases.[12] We have monitored the laser light scattered from the target with a fiber optic oriented at 30° with respect to the target normal. At low intensities, the reflected pulse shape was identical to the incident pulse shape. Above plasma formation threshold, a significant portion of the leading edge of the reflected pulse was removed. Therefore the total absorbed laser energy is not known.

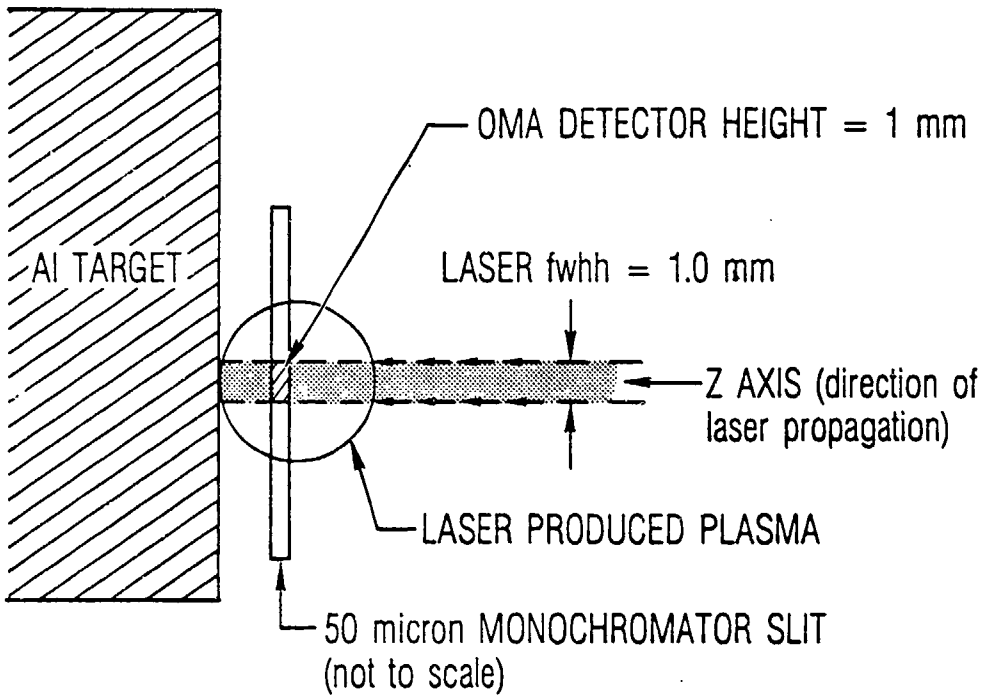

Fig. 3. OMA-monochromator field of view relative to target surface

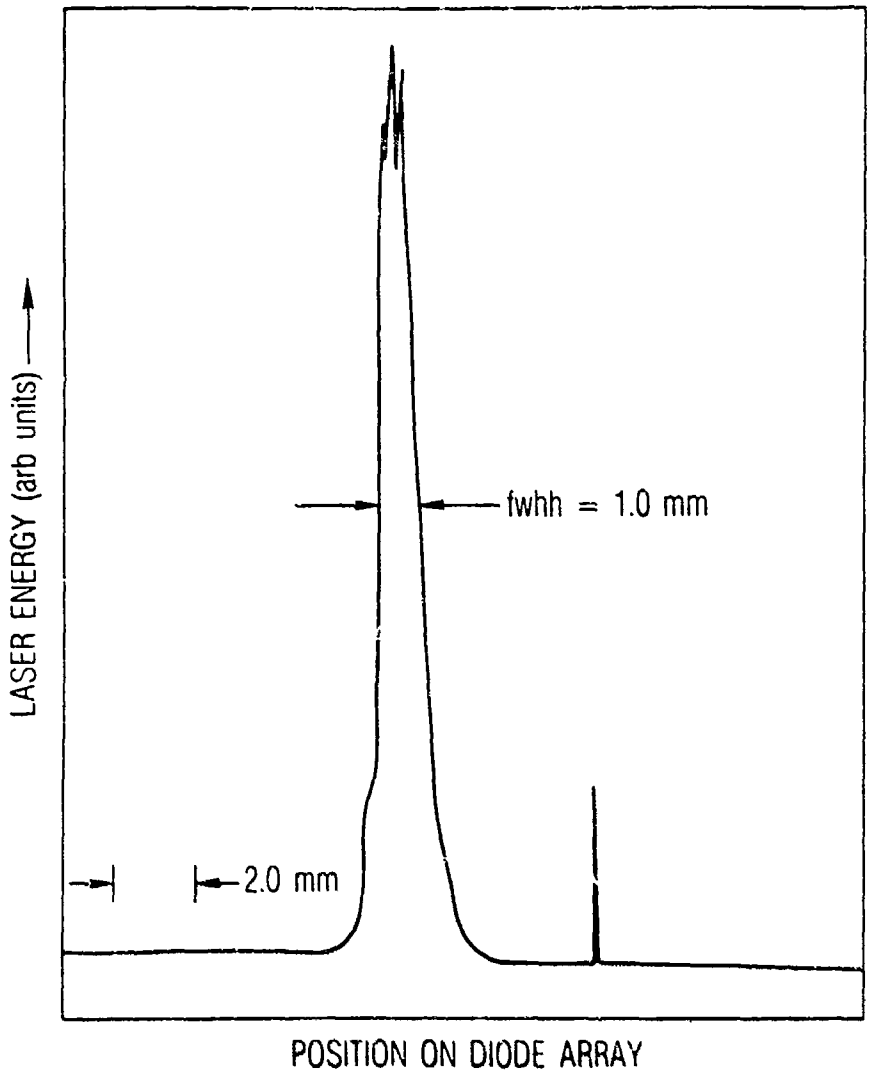

Fig. 4. Focused Beam Profile at Target Surface

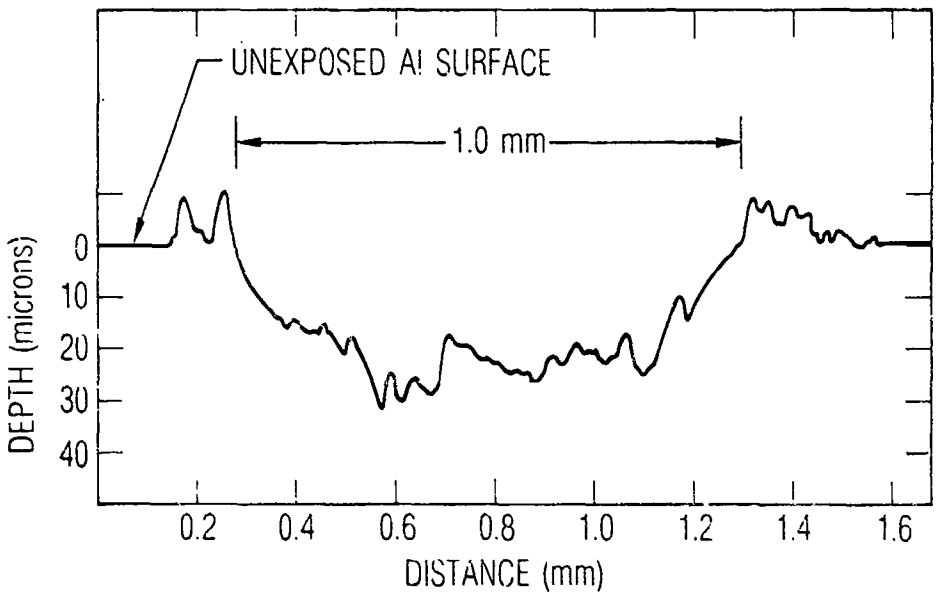

Fig. 5. Depth Profile of Laser-Produced Crater at Laser Intensity 5.3×10^7 W/cm^2

III. RESULTS

A. EMISSION SPECTRUM

The visible emission spectrum from the LPP was recorded at different delay times (with respect to the leading edge of the pulse) and distance z away from the target surface. The latter was controlled by moving the monochromator on precision translators. Figures 6 through 9 show the intensity-corrected emission spectrum at 1.0-μs delay time and 1.27 mm from the target surface. This delay time occurs just after the peak of the laser pulse.

The aluminum emission lines were assigned with the aid of relative intensities. In Figs. 6 through 9, the lines are labeled by degree of ionization and wavelength from Ref. 13. Some of the lines are overlapping multiplets and the wavelengths are, therefore, an average. One line, at 381.7 nm, could not be assigned to an aluminum transition. The small broad peak at 583 nm is scattered laser light. The vertical scales in Figs. 6 through 9 have been corrected for both filters used to remove second-order grating effects and the spectral response of the OMA detector. The spectral response correction was done in 40-nm segments, so there is an uncertainty of about 2 in comparing line intensities between different figures.

Almost all of the emission lines in Figs. 6 through 9 originated from the Al(II) and Al(III) ions. The exception is the resonance line (Al(I)) at 394.4 and 396.1 nm in Fig. 7. The other resonance lines, at 308.2 and 309.2 nm in Fig. 6, appear as an absorption in the background continuum. Similar but much weaker absorptions occur at other expected Al(I) wavelengths, such as 256.8 and 257.5 nm, and can only be observed on a greatly expanded vertical scale.

B. SPATIAL AND TEMPORAL DEPENDENCE OF PLASMA EMISSION

With a fixed delay time, the emission spectrum can be sampled as a function of distance from the target. Figure 10 shows the 460-nm region at increasing distances from the target (at 1-μs delay time). This spectral segment was chosen because it is intense and shows both Al(II) (466 nm) and Al(III) (452 nm) components.

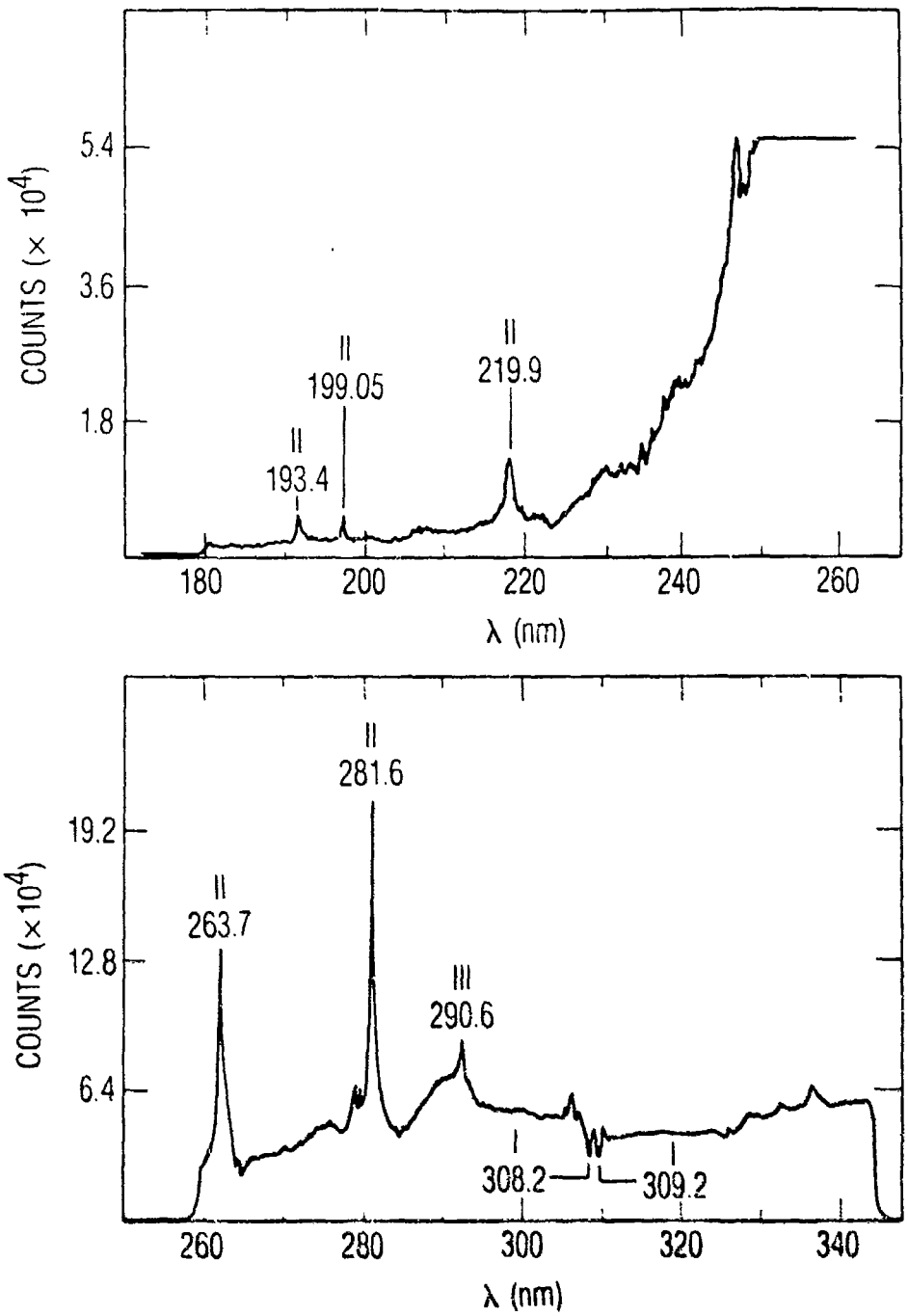

Fig. 6. Plasma Emission Spectrum from 180 nm to 340 nm at 5.3×10^7 W/cm^2, z = 1.27 mm, 1.0-μs Delay Time

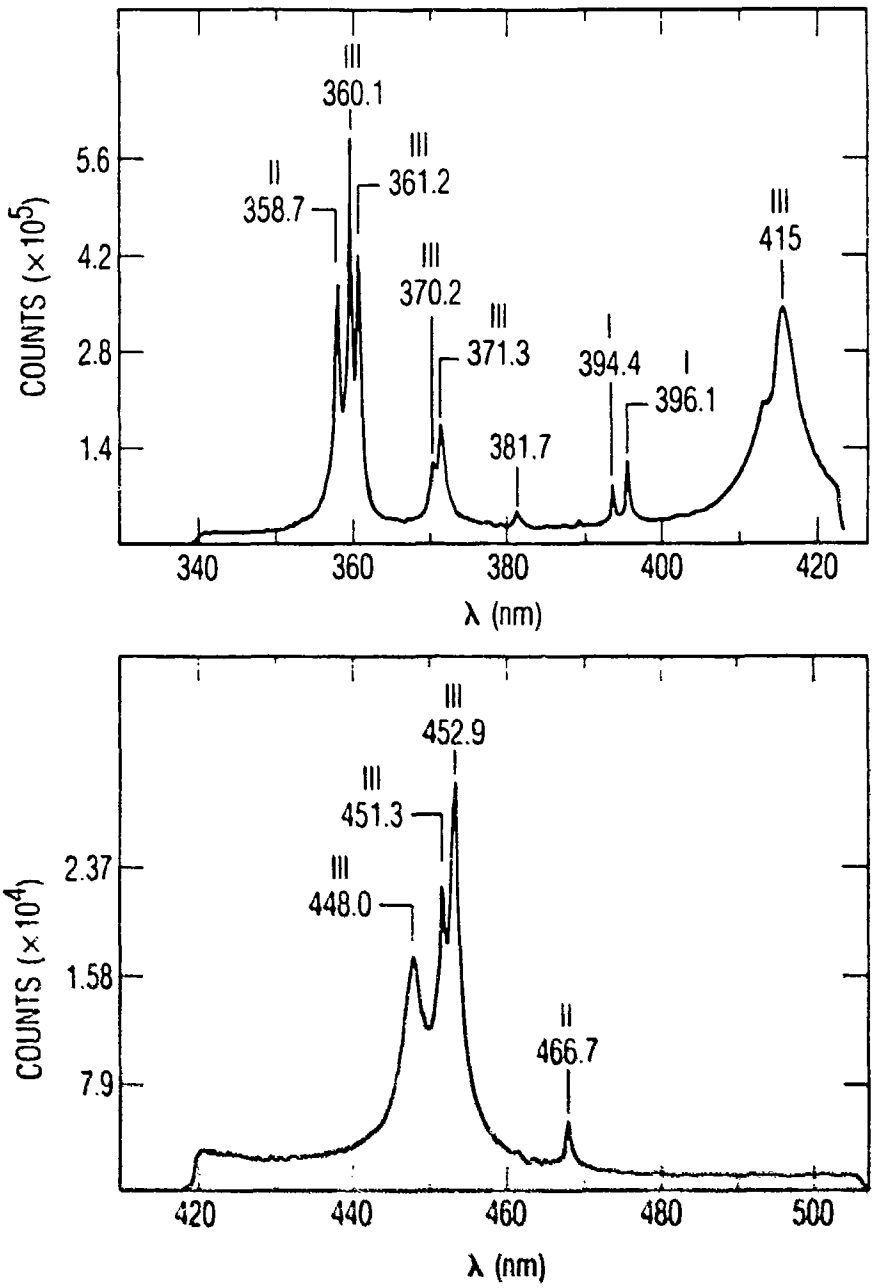

Fig. 7. Plasma Spectrum from 340 nm to 500 nm at 5.3×10^{7} W/cm^2, z = 1.27 mm, and 1.0-μs Delay Time

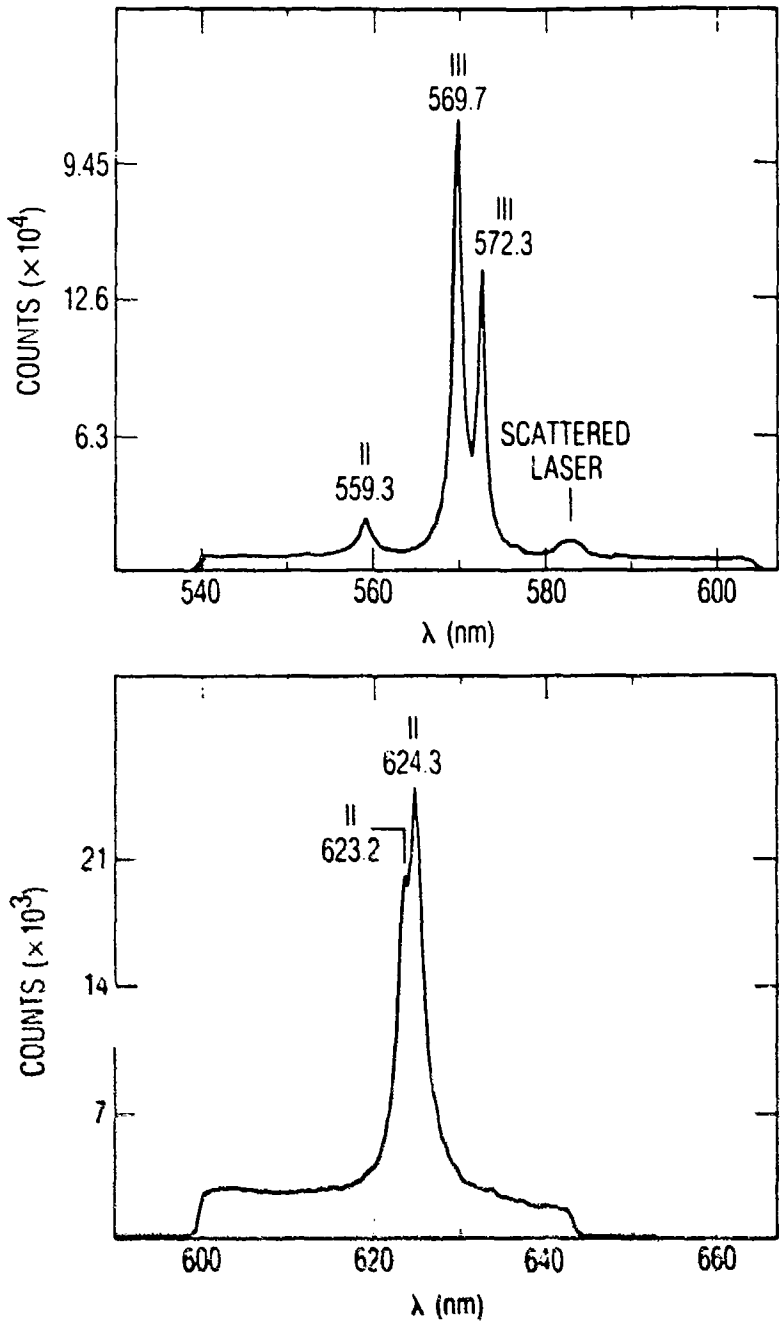

Fig. 8. Plasma Emission Spectrum from 540 nm to 640 nm at 5.3×10^7 W/cm^2, z = 127 mm, and 1.0-μs Delay Time

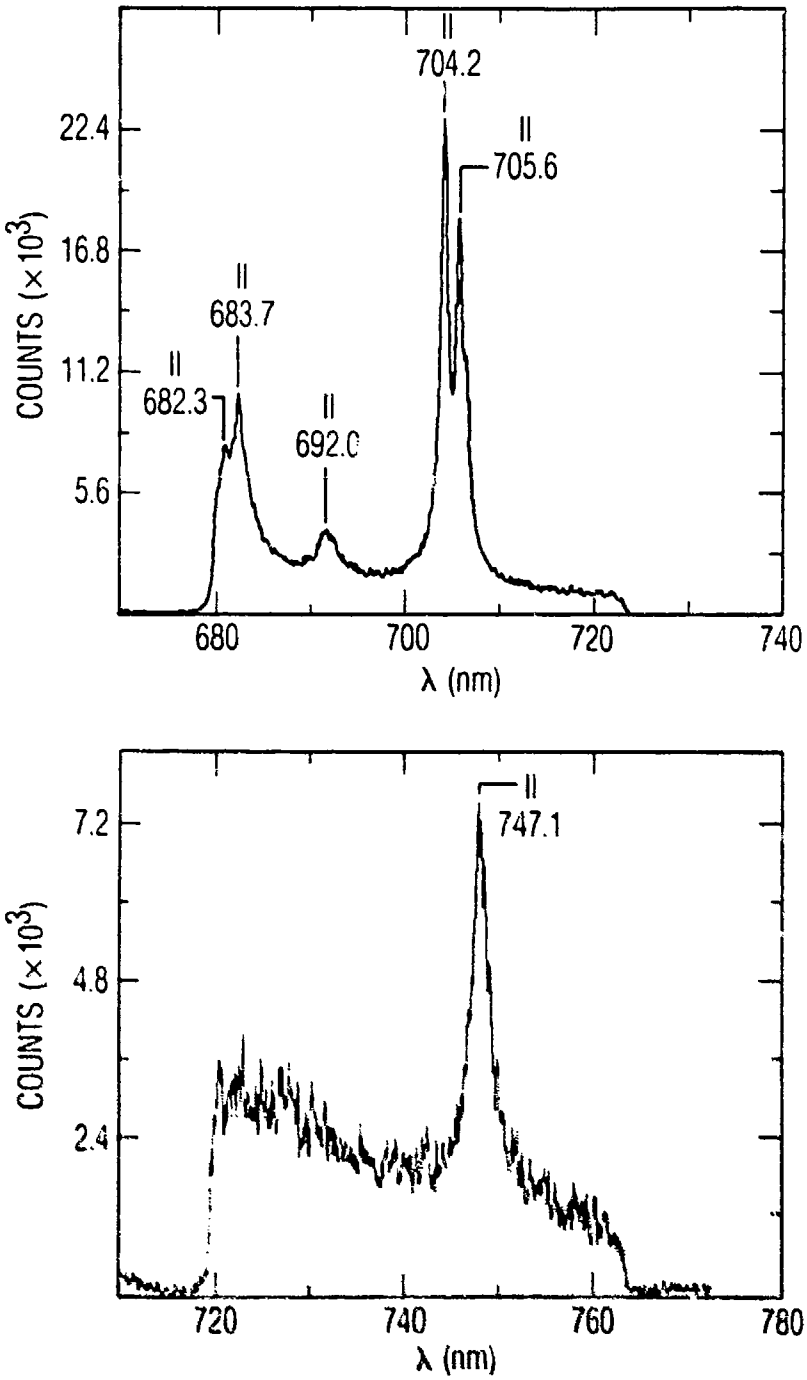

Fig. 9. Plasma Emission Spectrum from 680 nm to 760 nm at 5.3×10^7 W/cm^2, z = 1.27 mm, and 1.0-μs Delay Time

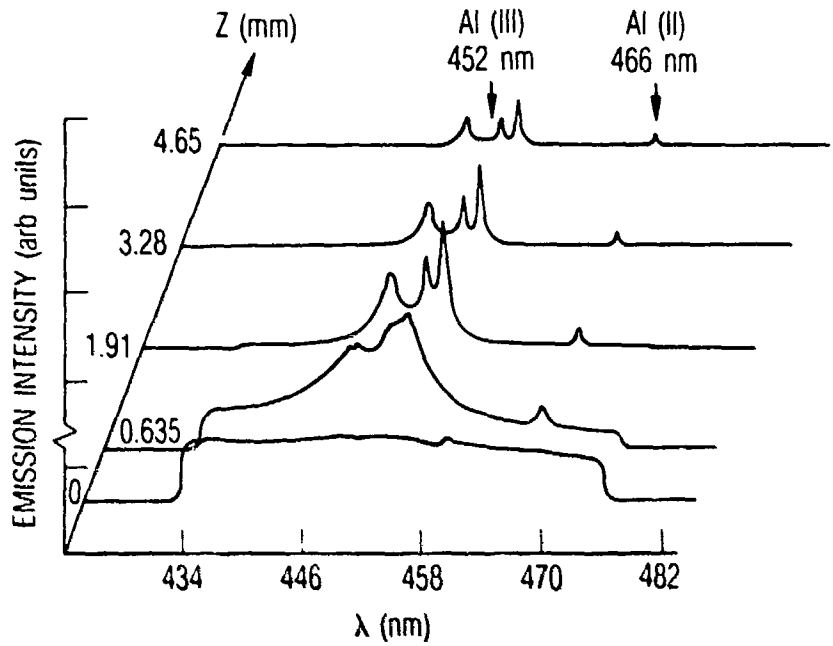

Fig. 10. Plasma Emission Spectrum in 460-nm Region at Five Distances z from Target Surface

In Fig. 10, the emission spectrum of the surface of the target, at z = 0, is an almost featureless continuum. At 0.635 mm from the target, the line emissions from Al(II) and Al(III) appear and are stronger than the continuum. At increasing distances from the target, the continuum decreases, and both the linewidths and intensities of the Al ion lines decrease.

Figure 11 shows the spatial distribution of Al(II) ions based on the areas under the 466-nm line as a function of distance from the target at two delay times: 0.2 and 1.0 μs. At the longer delay time, the LPP has propagated further along the z axis. An approximate velocity of the plasma leading edge can be obtained from the data in Fig. 11. Based on the change in position of the leading edge position at fwhh, the velocity is 1.2×10^5 cm/sec. Identical results were obtained for the Al(III) 452-nm transition. However, velocities different by almost a factor of 2 can be calculated using positions other than the fwhh.

C. ELECTRON TEMPERATURE FROM Al(II) EMISSION

When the conditions of a plasma are such that local thermodynamic equilibrium (LTE) applies, the populations of the bound states follow a Boltzmann distribution.[14] We will initially assume that LTE is an appropriate description in order to determine a temperature and electron density and subsequently explore this assumption.

Relative emissivities of lines from a given state of ionization can be used to calculate an electron temperature. The lines must be well resolved for accurate emissivities ϵ_{mn}, and the transition probabilities A_{mn} must be known. Since the populations of the excited states are given by the Boltzmann distribution, Eq. (1) describes their relative emissivity.[2,14]

$$\ln\left[\frac{\epsilon_{mn}}{g_m A_{mn} \nu_{mn}}\right] = \ln \frac{N}{Z} - \frac{E_m}{kT} \qquad (1)$$

For a transition from upper state m to lower state n, ν_{mn} is the frequency, E_m and g_m are the energy and degeneracy of the upper state, respectively, k is the Boltzmann constant, and T is the temperature. A plot of the quantity on the left-hand side (lhs) of Eq. (1) versus E_m has a slope of $-1/kT$. Therefore

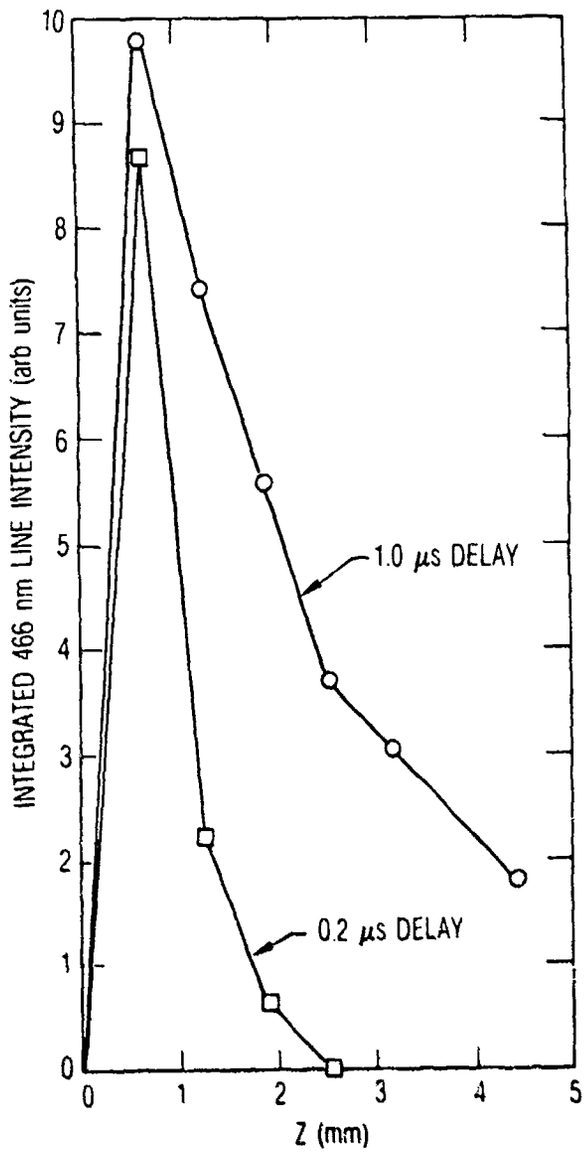

Fig. 11. Emissivity of 466-nm Al(II) Emission Line as a Function of Distance z from the Target for Two Delay Times: 0.2 and 1.0 μs

the temperature can be obtained without the total number density N or the partition function Z.

Five well-resolved transitions in the singlet manifold are shown in the energy level diagram of Al(II) in Fig. 12.[15] The upper level degeneracies and transition probabilities are given in Table I. Only relative emissivities (arbitrary units) are required for Eq. (1), and these were obtained by numerical integration of the OMA output (after conversion from wavelength units to frequency units) and corrected for OMA-monochromator sensitivity and filter transmissions. A plot of the lhs of Eq. (1) versus E_m is shown in Fig. 13 for $I_{laser} = 5.3 \times 10^7$ W/cm^2, 1.27 mm from the target surface and at 1-μs delay. The data fall on a straight line, indicative of LTE. A least squares fit yields a temperature of $8.13 \pm 0.27 \times 10^3$ K. Due to the dispersion of the monochromator, the relative emissivity of each transition required a separate laser pulse. The dye laser pulses were very reproducible, and the energy per pulse was constant to within a few percent over the five required pulses.

The electron temperature was measured at three lower laser intensities using neutral density filters to attenuate the laser. As shown in Table II, the laser intensity varied from 7×10^6 W/cm^2 (near LPP threshold) to 53×10^6 W/cm^2, but the Al(II) temperature remained essentially constant at 8.0×10^3 K to within one standard deviation. (At the lowest intensity, the monochromator slitwidth was increased to 200 μm due to the weak plasma emission.) However, several Al(III) emission features over the same laser intensity range are not constant and are indicative of increasing temperature with increasing intensity. Again, using the 460-nm region because it shows both Al(II) and Al(III) lines, Fig. 14 shows that the 452-nm Al(III) feature grows dramatically with increasing laser intensity. Identical behavior is observed when the Al(II) line at 559.3 nm is compared to the Al(III) line at 569.7 and 572.3 in Fig. 8.

As pointed out by Bekefi,[2] plasmas with steep density and temperature gradients can make ratios of intensities from different stages of ionization difficult to interpret. This is because emission from higher stages

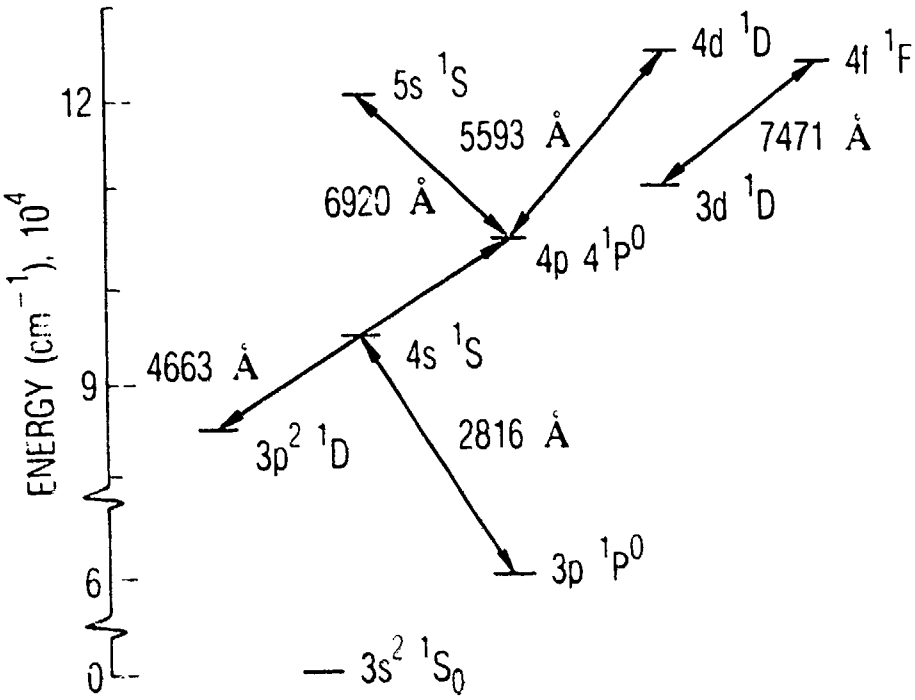

Fig. 12. Partial Energy-Level Diagram for Al(II) Showing Transitions Used for Temperature Calculations

Table I. Parameters for Electron Temperature Calculations

Species	Emission line (nm)	E_m [a] (cm^{-1})	g_m [a]	$A_{mn} \times 10^8$ (sec^{-1})	Corrected emissivity (arbitrary units)
Al(II)	281.6	95,351	1	3.83	3.47
Al(II)	466.3	106,921	3	0.53	4.54×10^{-1}
Al(II)	559.3	124,794	5	2.3	2.44×10^{-2}
Al(II)	692.0	121,367	1	0.96	3.42×10^{-2}
Al(II)	747.1	123,471	7	0.94	1.84×10^{-2}
Al(III)	370.2	170,637	2	3.42	0.56[b]
	371.3				
Al(III)	569.6	143,684	6	0.878	0.29[b]
	572.2				

[a]Reference 13.
[b]Emissivity for overlapping pairs; see text.

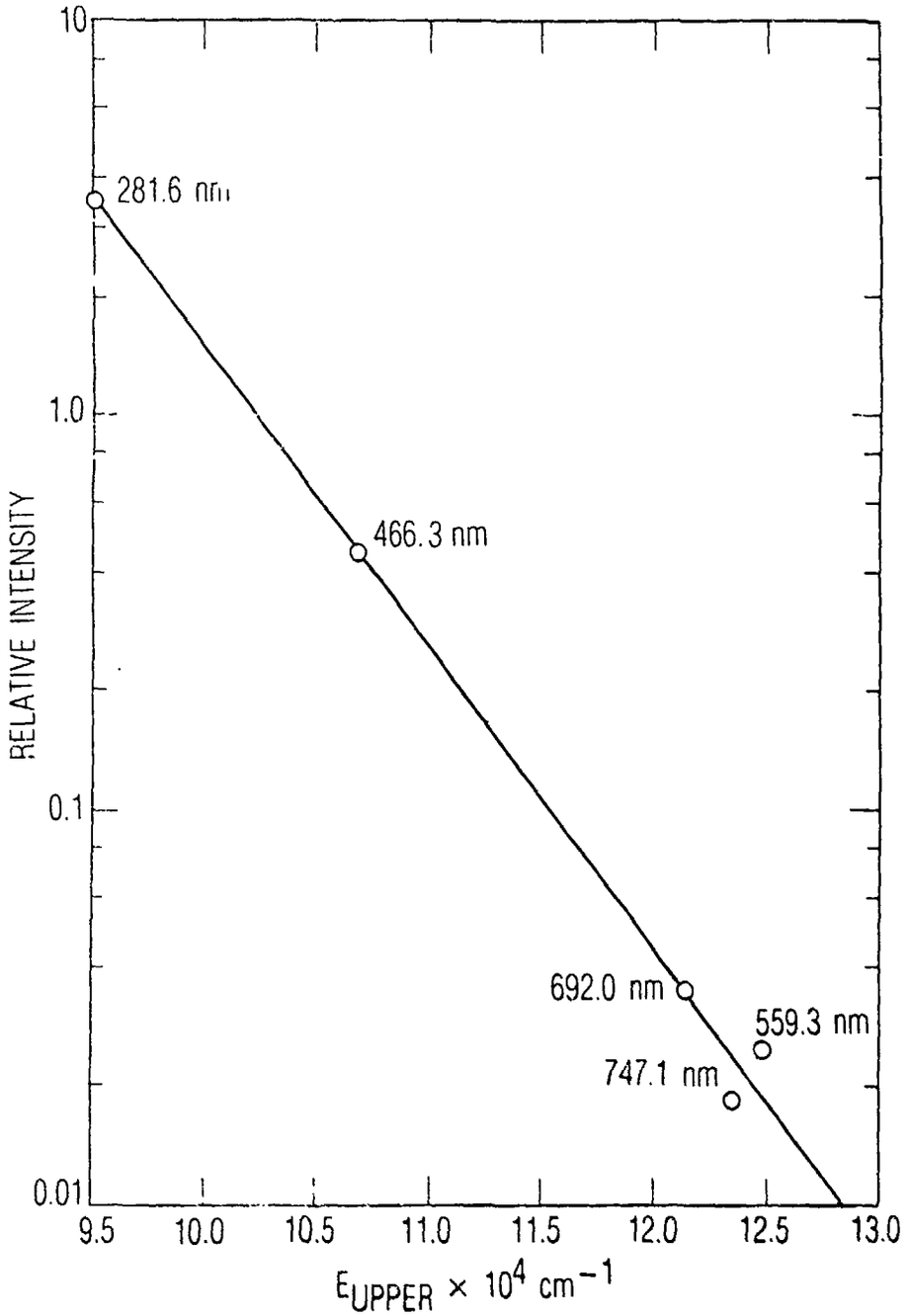

Fig. 13. Relative Emissivities Corrected for Degeneracy and Radiative Rate Versus Energy of Upper State. Temperature = $8.13 \pm 0.27 \times 10^3$ K, at 1.27 mm from target surface and 1-μs delay time; laser intensity = 5.3×10^7 W/cm^2.

Table II. Laser Intensity Dependence of T_e and N_e

Laser fluence (J/cm^2)	Laser intensity[a] (W/cm^2)	Temperature from Al(II) intensities[b] (K)	N_e[d] (cm^{-3})
105	5.3×10^7	$8.13 \pm 0.37 \times 10^3$	$3.3 \pm 0.3 \times 10^{17}$
45.9	2.3×10^7	$7.89 \pm 0.27 \times 10^3$	$3.9 \pm 0.4 \times 10^{17}$
25.9	1.3×10^7	$7.66 \pm 0.31 \times 10^3$	$3.5 \pm 0.4 \times 10^{17}$
14.3	7.2×10^6	$8.31 \pm 0.54 \times 10^3$[c]	-----

[a]Calculated using a pulse width of 2×10^{-6} μs.
[b]± one standard deviation.
[c]Measured with 200-μm monochromator slits.
[d]Derived from 466.3-nm Stark-broadened linewidth.

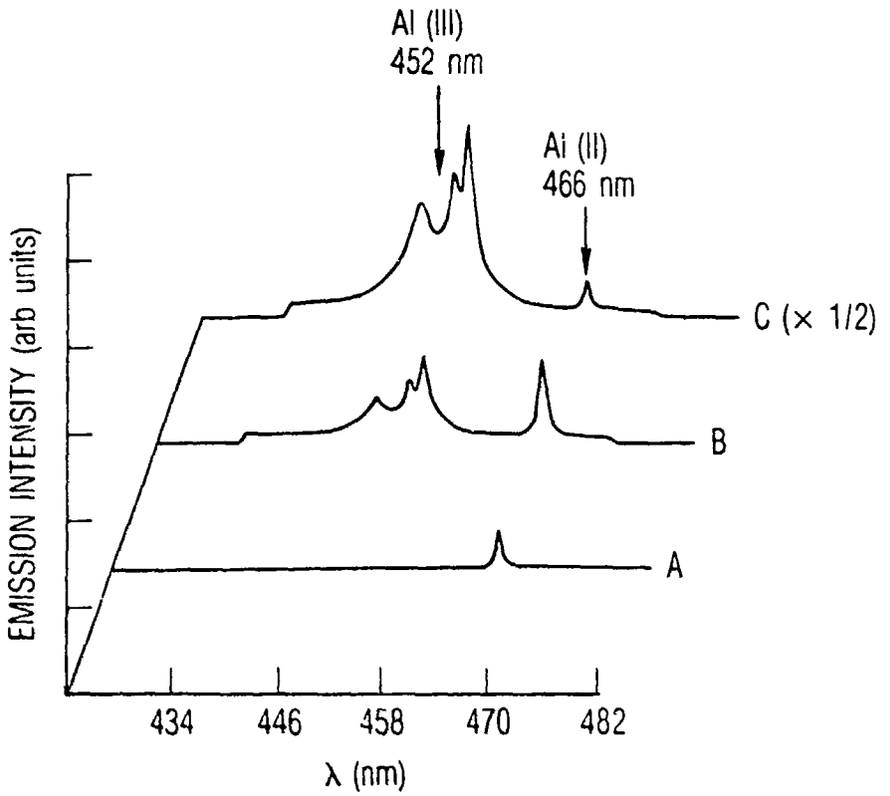

Fig. 14. The 460-nm Spectral Region at Three Laser Intensities: (A) 1.3×10^7 W/cm^2, (B) 2.3×10^7 W/cm^2, (C) 5.3×10^7 W/cm^2. The intensity of spectrum C has been decreased by one-half. Delay time is 1 μs, and the distance from the target is 1.27 mm.

of ionization can occur from cool outer layers. The homogeneity of the viewed plasma region was experimentally verified by placing a 50-μm pinhole immediately in front of the monochromator slit. The pinhole was scanned up and down the monochromator slit, corresponding to sampling different radial positions of the plasma. The ratio of the 452-nm to 466-nm emissivities was constant over a 1-mm region. Therefore, we conclude that the observed emissions from Al(II) and Al(III) originate from the same (homogeneous) region of the plasma.

D. ELECTRON DENSITIES

The linewidths of Al(II) transitions are primarily due to Stark broadening by the electrons.[14,16] For well-resolved transitions for which the Stark broadening coefficients have been measured or calculated, linewidth measurements can provide electron densities. Four lines of Al(II) were identified as candidates for electron density measurements: 466.3 nm, 559.3 nm, 691.8 nm, and 747.1 nm. Figure 15 shows the 466.3-nm line at sufficient resolution to measure the fwhh (6.1 Å). Since all four lines showed approximately Lorentzian line shapes, the correction for the instrumental line broadening was accounted for by Eq. (2), where $\Delta\lambda$ is the full width at half height (fwhh).[2]

$$\Delta\lambda_{true} = \Delta\lambda_{observed} - \Delta\lambda_{instrument} \tag{2}$$

Table III shows the observed linewidths, true (corrected) linewidths, and the standard deviation in the true linewidth based on five separate linewidth measurements over a four-month period. The 466.3-nm line had the best signal-to-noise ratio of the four transitions and the smallest standard deviation.

To a good approximation (~ 20 to 30%), $\Delta\lambda$ of a line is given by:

$$\Delta\lambda = 2W\left(\frac{N_e}{10^{16}}\right) + 3.5\,A\left(\frac{N_e}{10^{16}}\right)^{1/4}\left[1 - 1.2\,N_D^{-1/3}\right] W\left(\frac{N_e}{10^{16}}\right) \tag{3}$$

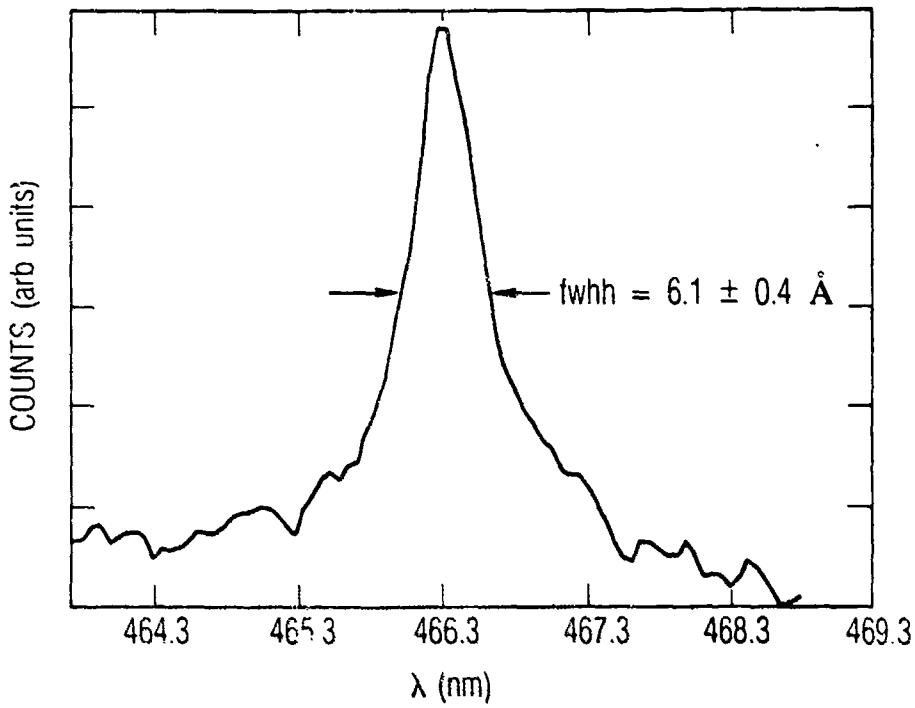

Fig. 15. The Al(II) 466.3-nm Emission Line at 1.27 mm from the Target Surface and 1-μs Delay Time; Laser Intensity = 5.3×10^7 W/cm^2

Table III. Stark Broadened Linewidths

Emission line (nm)	Linewidth $\Delta\lambda$ Observed[a] (nm)	Linewidth $\Delta\lambda$ True[b] (nm)	W (at 8000 K, $N_e = 10^{16}$ cm^{-3}) (nm)	A (at 8000 K)	N_e (cm^{-3})
466.3	0.649	0.419 ± 0.045	6.85×10^{-3}(c)	--	$3.1 \pm 0.3 \times 10^{17}$
559.3	1.62	1.39 ± 0.16	6.00×10^{-2}(d)	8.7×10^{-2}	$1.1 \pm 1.4 \times 10^{17}$
696.8	1.83	1.60 ± 0.44	1.04×10^{-2}(d)	5.6×10^{-2}	$7.7 \pm 2.1 \times 10^{17}$
747.1	1.65	1.42 ± 0.34	1.26×10^{-2}(d)	4.8×10^{-2}	$5.6 \pm 1.3 \times 10^{17}$

[a]Average of five measurements.
[b]Standard deviation derived from five measurements.
[c]From Reference 16.
[d]Interpolated from Reference 14.

where W is the electron impact width parameter and A is the ion-broadening parameter, both weak functions of temperature.[2] N_e is the electron density (cm^{-3}) and N_D is the number of particles in the Debye sphere as given by Eq. (4).

$$N_D = 1.72 \times 10^9 \frac{[T(eV)]^{3/2}}{[N_e(cm^{-1})]^{1/2}} \tag{4}$$

The broadening coefficients, W and A, given in Table II, are interpolated to 8000 K from values in Ref. 14. The contribution from ion broadening, given by the second term in Eq. (3), is very small, typically less than 0.01 nm for the conditions investigated here. Since the narrowest measured linewidth was 0.68 nm, the entire width can reasonably be ascribed solely to electron impact broadening. Therefore, electron densities can be calculated from just the first term in Eq. (3).

The last column in Table III contains the electron densities derived from the Stark broadened linewidths. The densities range from 1.1×10^{17} to 7.7×10^{17} cm^{-3} with an average of 4.4×10^{17} cm^{-3} (at 1-μs delay and z = 1.27 nm). The density based on the 466.3-nm line is the most reliable for two reasons. As is apparent from its low value of standard deviation, this measurement had the best signal/noise ratio of the four lines. In addition, the electron broadening parameter W has been experimentally verified. However, all four electron densities agreed within two standard deviations. The number of particles in the Debye sphere N_D is 1.8, based on the measured values of temperature and electron density.

The electron densities derived from the 466.3-nm linewidth as a function of laser intensity are shown in Table II. (At the lowest intensity, the slitwidths were too large for accurate linewidth measurements.) The electron densities are essentially constant over the laser intensity range of 1.3 to 5.3×10^7 W/cm^2. This is identical to the intensity dependence of the electron temperature.

E. TEMPERATURE AND ELECTRON DENSITIES AS A FUNCTION OF TIME AND POSITION

Analysis of the plasma emission provides the electron temperature and density as described previously. Figure 16 shows the variation of the temperature as a function of z, the distance from the target. The temperature ranges from approximately 8000 K at 0.67 mm to 7000 K at almost 7 mm, all measured at 1-μs delay time. The points are connected by lines for visualization, and the error bar is one standard deviation as derived from the least squares fit to the Boltzmann plots. At distances of less than one-half of a millimeter, the emission lines are so broad that they are not discernible from the continuum emission of the hot target (see Fig. 10). Also, in Fig. 16 the electron densities based on the 466.3-nm linewidth are shown. The error bar for the electron density was derived from the standard deviation shown in Table II. In Fig. 16 the electron density falls a factor of 10 in 7 mm, while the temperature remains almost constant (8000 K to 7000 K).

The time dependence of both the temperature and electron density at z = 1.27 mm is shown in Fig. 17. Both quantities rise to their long time (1-μs values) in less than 0.2 μs, the minimum delay time available. Since the risetime (0-100%) of the laser pulse is at least 0.6 μs (see Fig. 2), the temperature appears to "clamp" at an essentially constant value of about 8000 K from early in the risetime to the tail of the pulse at 3 μs. At times longer than 3 μs, there was insufficient emission intensity to obtain a temperature. The electron density shows the same rapid rise but drops to about one-half the peak value at 3 μs.

F. CONTINUUM EMISSION SPECTRUM AT z = 0 mm

Figure 18 shows an emission spectrum of the LPP taken as close to the target surface as possible. Although it was obtained at normal resolution (0.23 nm), it is plotted every 20 nm because it was almost featureless. Absorption features due to Al(I) at 308 nm (weak) and 395 nm (strong) were apparent, as well as weak emission from Al(III) at 360 nm. The data in Fig. 18 have been corrected for the spectral sensitivity as described earlier.

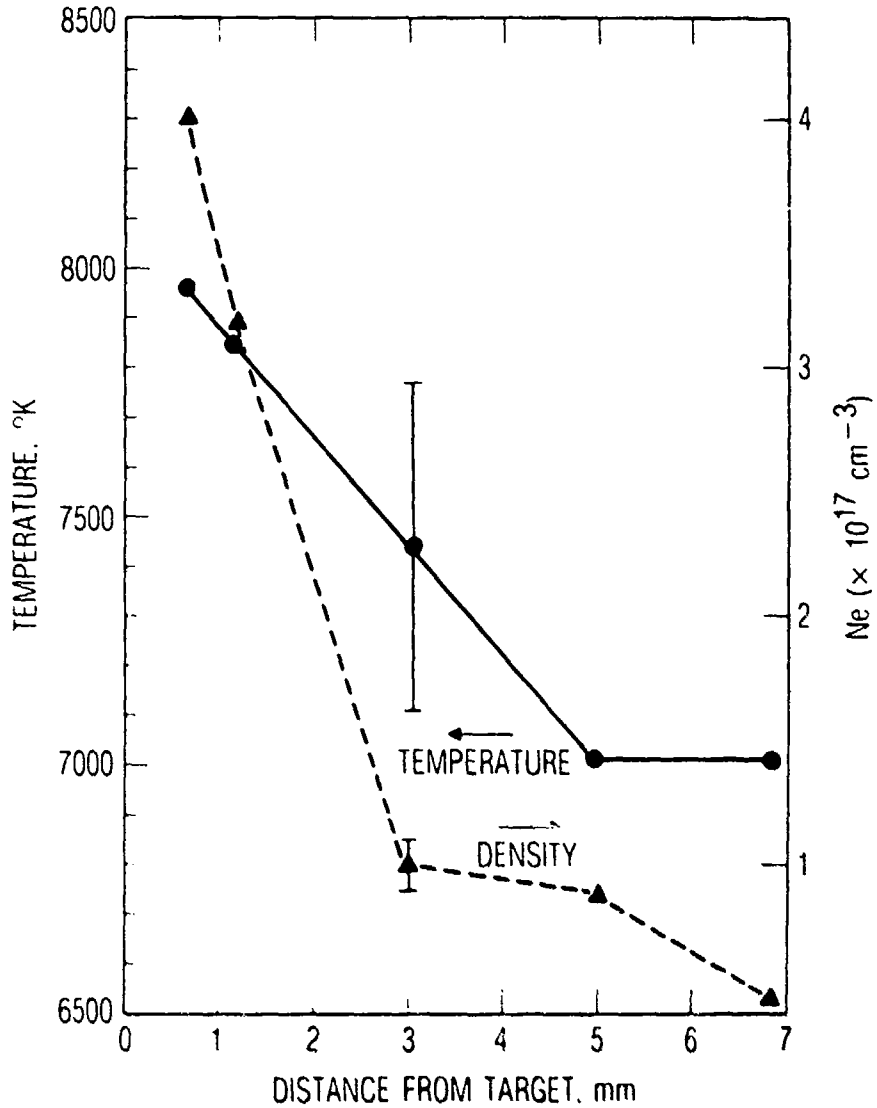

Fig. 16. Electron Temperature and Plasma Electron Densities Derived from the Stark-Broadened 466.3-nm Line as a Function of Distance z from the Target: Laser Intensity = 5.3×10^7 W/cm^2 at 1-μs Delay Time

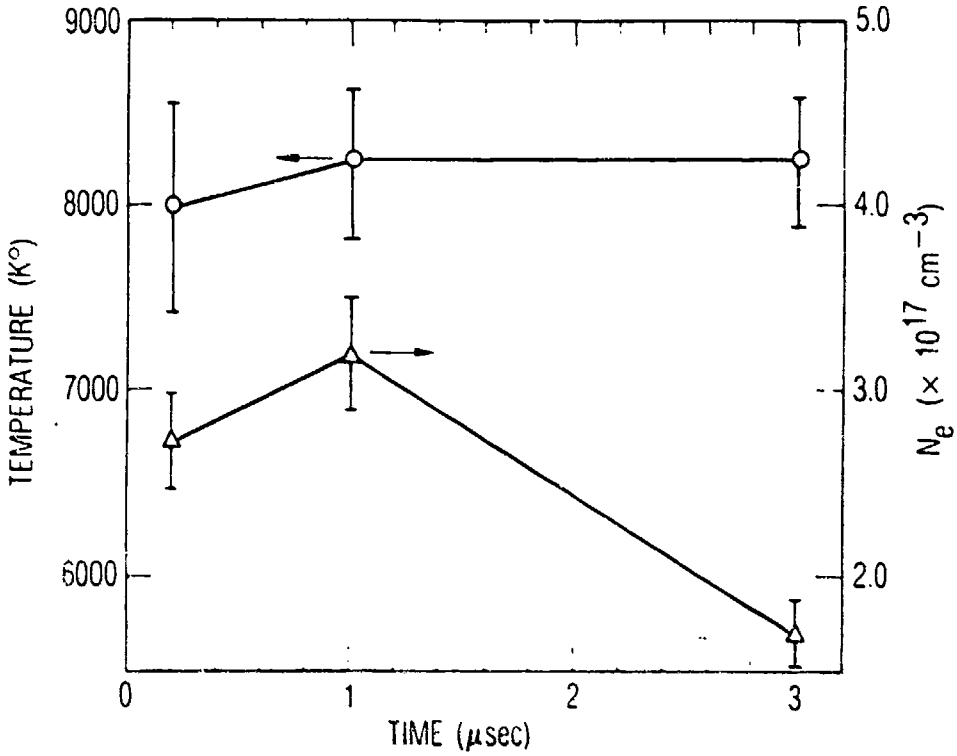

Fig. 17. The Al(II) Temperature and Electron Density Derived from the 466.3-nm Stark-Broadened Linewidth at Three Delay Times. Laser intensity = 5.3×10^7 W/cm^2 and 1.27 mm from target surface.

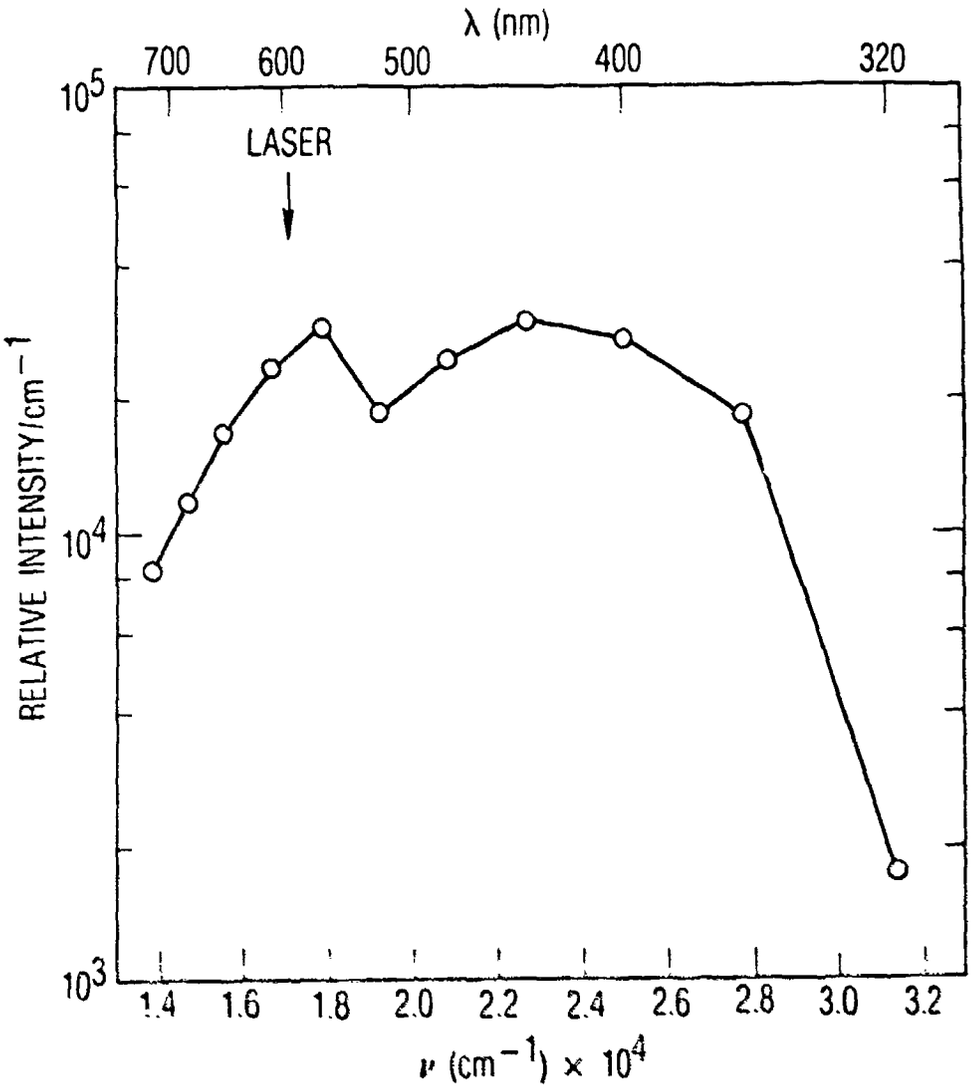

Fig. 18. Plasma Emission Spectrum at 5.3×10^7 W/cm^2, 0 mm from Target Surface, 1-μs Delay Time

Continuum emission is produced by both free-free bremsstrahlung (presumably electron collisions with atoms) and recombination radiation accompanying electron-ion recombination. The latter process appears to be responsible for the dip in emission intensity at 1.9×10^4 cm^{-1} (2.4 eV). The recombination process produces a photon with energy equal to the energy difference between Al^+ and Al^* plus the kinetic energy of the electron:

$$Al^+ + e^- \longrightarrow Al^* + h\nu$$

$$h\nu = E_{Al^+} - E_{Al^*} + K.E.(e^-)$$

The ionization potential of Al(5.98 eV) must be adjusted for the lowering due to the collective coulombic plasma interactions ($\Delta\chi_i$) that depend on the cube root of the electron density (using the Unsöld formula). We can estimate N_e near the target surface by extrapolating the N_e versus z data in Fig. 16. At $N_e = 5 \times 10^{17}$ cm^{-3} we calculate $\Delta\chi_i = 0.55$ eV.[17] N_e is only an estimate because the detector probably views a region with steep N_e gradients and the distance from the target surface is not accurately known (± 0.2 mm). However, the weak dependence of $\Delta\chi_i$ on N_e reduces the error.

The recombination process will produce emission with a low frequency cut-off corresponding to the capture of an electron with zero kinetic energy. This cut-off frequency corresponds to the energy difference between the product excited state and the corrected ionization potential. We can now calculate the energy of Al^*.

$$E_{Al^*} = E_{Al^+} - h\nu = 5.43 \text{ eV} - 2.4 \text{ eV} = 3.0 \text{ eV}$$

The lowest excited state of Al is $4\ s^2S$ at 3.14 eV. Since the uncertainty in the position of the dip in Fig. 18 is about 0.1 eV (± 20 nm), recombination of Al^+ to form $Al(4\ s^2S)$ appears to be a reasonable explanation for its origin.

IV. DISCUSSION

In LTE plasmas, the populations of atomic and ionic excited states are maintained by electron collisions. Since the collision frequency is proportional to the electron density, a lower limit for the electron density given in Eq. (5) has been determined that will maintain the populations to within 10% of LTE.[1]

$$N_e(cm^{-3}) \geq 1.6 \times 10^{12}\ T^{1/2}\ (K)\ [\Delta E\ (eV)]^3 \qquad (5)$$

ΔE is the energy difference between the upper and lower states, and T is the temperature. Using $\Delta E = 4.5$ eV, corresponding to the largest energy gap of the five transitions (281.6 nm) used for temperature measurements, the lower limit given by Eq. (5) is $1.3 \times 10^{16}\ cm^{-3}$. Our measured N_e values generally exceed this by a factor of 10. Additional support for LTE is the agreement between the experimentally measured line intensities and the Boltzmann distribution [Eq. (2)] as seen in Fig. 13.

As described in section III-C, the electron temperatures derived from Al(II) lines were found to be independent of laser intensity, while the emission from several Al(III) lines decreased rapidly with decreasing laser intensity. To investigate this different behavior, we make quantitative estimates of Al(III) concentrations based on Al(III) emission lines.

There are no well-resolved Al(III) transitions. However, two pairs of Al(III) lines that are overlapping may be used to gain information about the Al(III) species. As can be seen in Figs. 7 and 8, there are two pairs of Al(III) multiplets at 370.2 and 371.3 nm and 569.6 and 572.2 nm, respectively. They represent emission from a three-level system in which the intermediate state is split by spin-orbit interaction. The 370-nm pair arises from a $5\ ^2S\ 1/2 \rightarrow 4\ ^2P_{1/2,3/2}$ transition in which the lower level is split by 80 cm^{-1}. This split level is the upper level for the 570-nm pair; $4\ ^2P_{1/3,3/2} \rightarrow 4\ ^2S_{1/2}$. Since the spin orbit splitting between the $^2P_{1/2,3/2}$ states is much smaller than kT (7000 cm^{-1}), we will assume that they are

closely coupled by collisions and treat the two spin-orbit states as one. The measured relative line emissivities for these two Al(III) pairs, as given in Table 1, are inverted compared to equilibrium expectations. That is, there is apparently more emission from the higher lying 5 $^2S_{1/2}$ state than the lower lying 4 $^2P_{1/2,3/2}$ states.

Another approach is to compare the relative emissivities between Al(II) and Al(III) species. With our measured values for electron density and temperature, the Saha equation can be used to calculate the relative concentrations of the Al(II) and Al(III). At 1.27 mm from the target surface ($T = 8.0 \times 10^3$ K, $N_e = 3.0 \times 10^{17}$ cm^{-3}), the relative concentrations are Al(II)/Al(I) = 1.6 and Al(II)/Al(III) = 1.0×10^{-6}, using the partition function and coulombic plasma interactions parameters of Ref. 17. (The ionization potentials are Al(I) = 5.986 eV and Al(II) = 18.828 eV.) As shown in Table I, the radiative rates and degeneracies of the observed Al(II) and Al(III) states are approximately the same. Therefore, based simply on the million to one relative concentrations, we would not expect to see any Al(III) emission.

A more quantitative calculation of the expected relative emissivities can be made using Eq. (6).[2]

$$\frac{\epsilon_1}{\epsilon_2} = \frac{\lambda_2}{\lambda_1} \frac{g_n(1)}{g_n(2)} \frac{A(1)}{A(2)} \left(\frac{kT}{\lambda_H}\right)^{3/2} \frac{\exp(-\Delta E/kT)}{4\pi^{3/2} a_o^3 N_e} \tag{6}$$

All the variables in Eq. (6) have the same definition as in Eq (2) except that the numeral 1 denotes the higher stage of ionization and a_o is the Bohr radius (5.29×10^{-9}cm), λ_H is the ionization energy of hydrogen (13.595 eV), and N_e is the electron density (cm^{-3}). ΔE is the difference in excitation energies plus the ionization energy of the lower stage of ionization in the plasma.

$$\Delta E = [E(1) - E(2)] + [\chi_i - \Delta\chi_i]$$

Using the information in Table I and Ref. 17 (for lowering of the ionization energy by collective plasma interactions $\Delta\chi_i$), we have calculated the ratio of

emissivities for the Al(III) lines (again treating the overlapping multiplets as a single line) relative to the Al(II) 466.3-nm line (the strongest Al(II) line). These ratios are exceedingly small: 370 nm/466.3 nm = 5×10^{-12} and 570 nm/466.3 nm = 1.3×10^{-10}. These ratios are smaller than the ratios from the Saha predictions due primarily to the excitation energies of the excited states.

We conclude that Al(II) and Al(III) concentrations are not in equilibrium at 1.27 mm from the target and 1-μs delay time. We speculate that the Al ions are not produced in equilibrium concentrations in the target-laser interaction region. This could occur if nonthermal ionization (i.e., photoionization) mechanisms are important. The significance of the photoionization step has been noted by Rosen et al. in their modeling of the dependence of the plasma threshold on the laser (λ = 0.35 μm) pulsewidth.[8] Their threshold model agreed with experimental results only when photoionization of excited Al atoms was included.

Another important plasma consideration is that the absorption by inverse bremsstrahlung processes be sufficiently small that the plasma is optically thin in the observed regions. This will occur when the optical frequency is much higher than the plasma frequency ν_p. ν_p depends on the square root of the electron density N_e.[1]

$$\nu_p = 8.9 \times 10^3 \, N_e^{1/2}$$

In the region of highest electron density (z = 0.635 mm), $N_e = 3.0 \times 10^{17} cm^{-3}$ and $\nu_p = 4.9 \times 10^{12}$ sec^{-1}. Since the lowest optical frequencies observed (800 nm = 3.8×10^{14} sec^{-1}) were almost one hundred times greater than the plasma frequency, the plasma should be optically thin. Of course this is not true for frequency regions corresponding to transitions originating from the ground state of Al(I). Indeed, absorptions due to Al(I) were observed at 309 nm.

The plasma parameters determined by the techniques reported here may be compared to hydrodynamic models. In such a comparison the homogeneity of the

blow-off is of interest. We used a glass microscope slide placed 2 cm from the target surface and as near as possible to the incident laser beam to collect the blow-off material from 20 laser shots. A 390X optical microscope revealed sparsely spaced, circular droplets with diameters of several microns. The same droplets were observed with a 1000X to 3000X SEM. In the energy resolved mode, the SEM identified the deposits as aluminum. It also showed significant amounts of aluminum deposited between the observable droplets, presumably corresponding to deposited atomic vapor. It was not possible to estimate the relative amounts, but it is apparent that the blow-off is made up of both atomic vapor and droplets.

V. CONCLUSIONS

The spatially and temporally resolved emission spectrum of an aluminum LPP has lead to N_e and T_e as a function of time and space for incident laser intensities from near threshold to 5×10^7 W/cm^2. The same techniques are applicable to higher incident laser intensities. An upper limit for the T_e technique can be estimated. As T_e increases, the slope of the Boltzmann plot decreases. If we take the minimum acceptable slope as 2, then the temperature derived from the five lines reported here yields T_e = 5.4 eV. There are several lines below 250 nm that could have been included in an Al(II) Boltzmann plot (but were not included because of difficulty with intensity calibration in this region) that would have increased the maximum measurable temperature to 7.2 eV. Since T_e scales approximately as the cube root of the incident intensity, this technique should be applicable to incident laser intensities of up to 10^{10} W/cm^2. An upper limit for the electron density technique is more difficult to estimate. The linewidth at high N_e can be so large that the line is lost in the continuum emission. $N_e = 10^{18}$ cm^{-3} and probably $N_e = 10^{19}$ cm^{-3} are measurable if the line emission is comparable to the bremsstrahlung and recombination continuum emission.

REFERENCES

1. J. F. Ready, Effects of High-Power Laser Radiation (Academic Press, NY, 1971).

2. G. Bekefi, Principles of Laser Plasmas (John Wiley & Sons, NY, 1976).

3. T. P. Hughes, Plasmas and Laser Light (Adam Hilger, London, 1975).

4. R. W. Mitchel, R. W. Conrad, E. L. Roy, D. Keefer and C. W. Mathews, "The Role of Radiative Transfer in Pulsed Laser Plasma-Target Interactions," J. Quant. Spectrosc. Radiat. Transfer 20, 519 (1978).

5. C. T. Walters, R. H. Barnes and R. E. Beverly III, "Initiation of Laser-Supported-Detonation Waves," J. Appl. Phys. 49, 2937(1978).

6. J. A. McKay, R. D. Bleach, D. J. Nagel, J. T. Schriempf, R. B. Hall, C. R. Pond and S. K. Manlief, "Pulsed-CO_2-Laser Interaction with Aluminum in Air: Thermal Response and Plasma Characteristics," J. Appl. Phys. 50, 3231 (1979).

7. J. E. Rothenberg and G. Koren, "Laser Produced Plasma in Crystalline α - Al_2O_3 and Al Metal," App. Phys. Lett. 44, 667 (1984).

8. D. I. Rosen, J. Mitteldorf, G. Kothanduraman, A. N. Pirri and E. R. Pugh, "Coupling of Pulsed .35 Micron Laser Radiation to Aluminum Alloys," J. Appl. Phys. 53, 3190 (1982).

9. D. Rosen, G. Weyl, D. Hastings, and J. Mittledorf, "Coupling of Pulsed .35 Micron Laser Radiation to Metal Surfaces in Vacuum," Excimer Lasers, Their Application, and New Frontiers In Lasers, Proc. SPIE 476, 118 (1984).

10. B. C. Boland, F. E. Irons, and R. W. P. McWhirter, "A Spectroscopic Study of the Plasma Generated by a Laser from Polyethylene," J. Phys. B. (Proc. Phys. Soc), 1, 1180 (1968).

    F. E. Irons, R. W. P. McWhirter, and N. J. Peacock, "The Ion and Velocity Structure in a Laser Plasma," J. Phys. B: Atom. Molec. Phys. 5, 1975 (1972).

    F. E. Irons, "Stark Broadening of High Quantum Number $\Delta n = 1$ Transitions of Carbon V and VI in a Laser-Produced Plasma," J. Phys. B: Atom. Molec. Phys. 6, 1562 (1973).

    F. E. Irons and N. J. Peacock, "A Spectroscopic Study of the Recombination of C^{6+} to C^{5+} In An Expanding Laser-Produced Plasma," J. Phys. B: Atom. Molec. Phys. 1, 2084 (1974).

11. R. Stair, W. E. Schneider, and J. K. Jackson, "A New Standard of Spectral Irradiance," App. Opt. 2, 1151 (1963).

12. T. E. Zavecz, M. A. Saifi, and M. Notis, "Metal Reflectivity Under High Intensity Optical Radiation," App. Phys. Lett. 26, 165 (1975).

13. J. Reader, C. H. Corliss, W. L. Wiese, and O. A. Martin, Wavelength and Transition Probabilities for Atoms and Atomic Ions (NSRDS-NBS 68, U.S. Government Printing Office, 1980).

W. L. Wiese, M. W. Smith, and B. M. Miles, Atomic Transition Probabilities Vol. II Sodium Through Calcium (A Critical Data Compilation) (NSRDS-NBS 22, U.S. Government Printing Office, 1969).

14. H. R. Griem, Plasma Spectroscopy (McGraw-Hill, NY 1964).

15. S. Bashkin and J. O. Stoner, Jr., Atomic Energy Levels and Grotrian Diagrams, Vol. I (North-Holland, Amsterdam, 1975).

16. A. W. Allen, M. Blaha, W. W. Jones, A. Sanchez, and H. R. Griem, Phys. Rev. A 11, 477 (1975).

17. H. W. Drawin and P. Felenbok, Data For Plasmas In Local Thermodynamic Equilibrium (Gauthier-Villars, Paris, 1965).

LABORATORY OPERATIONS

The Aerospace Corporation functions as an "architect-engineer" for national security projects, specializing in advanced military space systems. Providing research support, the corporation's Laboratory Operations conducts experimental and theoretical investigations that focus on the application of scientific and technical advances to such systems. Vital to the success of these investigations is the technical staff's wide-ranging expertise and its ability to stay current with new developments. This expertise is enhanced by a research program aimed at dealing with the many problems associated with rapidly evolving space systems. Contributing their capabilities to the research effort are these individual laboratories:

Aerophysics Laboratory: Launch vehicle and reentry fluid mechanics, heat transfer and flight dynamics; chemical and electric propulsion, propellant chemistry, chemical dynamics, environmental chemistry, trace detection; spacecraft structural mechanics, contamination, thermal and structural control; high temperature thermomechanics, gas kinetics and radiation; cw and pulsed chemical and excimer laser development including chemical kinetics, spectroscopy, optical resonators, beam control, atmospheric propagation, laser effects and countermeasures.

Chemistry and Physics Laboratory: Atmospheric chemical reactions, atmospheric optics, light scattering, state-specific chemical reactions and radiative signatures of missile plumes, sensor out-of-field-of-view rejection, applied laser spectroscopy, laser chemistry, laser optoelectronics, solar cell physics, battery electrochemistry, space vacuum and radiation effects on materials, lubrication and surface phenomena, thermionic emission, photosensitive materials and detectors, atomic frequency standards, and environmental chemistry.

Computer Science Laboratory: Program verification, program translation, performance-sensitive system design, distributed architectures for spaceborne computers, fault-tolerant computer systems, artificial intelligence, microelectronics applications, communication protocols, and computer security.

Electronics Research Laboratory: Microelectronics, solid-state device physics, compound semiconductors, radiation hardening; electro-optics, quantum electronics, solid-state lasers, optical propagation and communications; microwave semiconductor devices, microwave/millimeter wave measurements, diagnostics and radiometry, microwave/millimeter wave thermionic devices; atomic time and frequency standards; antennas, rf systems, electromagnetic propagation phenomena, space communication systems.

Materials Sciences Laboratory: Development of new materials: metals, alloys, ceramics, polymers and their composites, and new forms of carbon; nondestructive evaluation, component failure analysis and reliability; fracture mechanics and stress corrosion; analysis and evaluation of materials at cryogenic and elevated temperatures as well as in space and enemy-induced environments.

Space Sciences Laboratory: Magnetospheric, auroral and cosmic ray physics, wave-particle interactions, magnetospheric plasma waves; atmospheric and ionospheric physics, density and composition of the upper atmosphere, remote sensing using atmospheric radiation; solar physics, infrared astronomy, infrared signature analysis; effects of solar activity, magnetic storms and nuclear explosions on the earth's atmosphere, ionosphere and magnetosphere; effects of electromagnetic and particulate radiations on space systems; space instrumentation.